nature plants

Resource

https://doi.org/10.1038/s41477-024-01683-2

A spatial transcriptome map of the developing maize ear

Received: 8 June 2023

Accepted: 3 April 2024

Published online: 14 May 2024

Check for updates

Yuebin Wang[1,9], Yun Luo[1,9], Xing Guo[2,3,9], Yunfu Li[1,9], Jiali Yan[1,9], Wenwen Shao[2,3,4], Wenjie Wei[1], Xiaofeng Wei[2,5], Tao Yang[2,5], Jing Chen[2,5], Lihua Chen[2], Qian Ding[1], Minji Bai[1], Lin Zhuo[1], Li Li[2], David Jackson[1,6], Zuxin Zhang[1,7], Xun Xu[2], Jianbing Yan[1,7], Huan Liu[2,8] ✉, Lei Liu[1,7] ✉ & Ning Yang[1,7] ✉

A comprehensive understanding of inflorescence development is crucial for crop genetic improvement, as inflorescence meristems give rise to reproductive organs and determine grain yield. However, dissecting inflorescence development at the cellular level has been challenging owing to a lack of specific marker genes to distinguish among cell types, particularly in different types of meristems that are vital for organ formation. In this study, we used spatial enhanced resolution omics-sequencing (Stereo-seq) to construct a precise spatial transcriptome map of the developing maize ear primordium, identifying 12 cell types, including 4 newly defined cell types found mainly in the inflorescence meristem. By extracting the meristem components for detailed clustering, we identified three subtypes of meristem and validated two MADS-box genes that were specifically expressed at the apex of determinate meristems and involved in stem cell determinacy. Furthermore, by integrating single-cell RNA transcriptomes, we identified a series of spatially specific networks and hub genes that may provide new insights into the formation of different tissues. In summary, this study provides a valuable resource for research on cereal inflorescence development, offering new clues for yield improvement.

Plant meristems harbour a population of pluripotent stem cells and their descendants, which are organized into distinct domains with specific functions. In flowering plants, meristems establish inflorescence architecture, and in crop species, they contribute to the determination of grain yield[1]. The inflorescence is initiated when a vegetative shoot apical meristem transitions into the inflorescence meristem (IM)[2]. In maize, the IM then proliferates and produces lateral meristems called spikelet pair meristems, which develop into spikelet meristems and then floral meristems[3]. Forward and reverse genetic approaches have identified over 150 genes that regulate inflorescence architecture in maize, such as *KNOTTED1* (ref. 4), *BARREN STALK1* (ref. 5), *RAMOSA1* (ref. 6), *RAMOSA3* (ref. 7), *BRANCHED SILKLESS1* (ref. 8), Zm*ACO2* (ref. 9) and *YIGE1* (ref. 10). However, genetic pleiotropy and redundancy still limit the insights into inflorescence gene regulatory networks[11].

Conventional transcriptomics approaches generate profiles of whole plant organs or tissues and ignore cell heterogeneity, making it difficult to address many biological problems[12]. With the rapid development of cell capture technology, single-cell transcriptome sequencing

[1]National Key Laboratory of Crop Genetic Improvement, Huazhong Agricultural University, Wuhan, China. [2]State Key Laboratory of Agricultural Genomics, Key Laboratory of Genomics, Ministry of Agriculture, BGI Research, Shenzhen, China. [3]BGI Research, Wuhan, China. [4]College of Life Sciences, University of Chinese Academy of Sciences, Beijing, China. [5]China National GeneBank, Shenzhen, China. [6]Cold Spring Harbor Laboratory, Cold Spring Harbor, NY, USA. [7]Hubei Hongshan Laboratory, Wuhan, China. [8]Guangdong Laboratory of Lingnan Modern Agriculture, Agricultural Genomics Institute at Shenzhen, Shenzhen, China. [9]These authors contributed equally: Yuebin Wang, Yun Luo, Xing Guo, Yunfu Li, Jiali Yan. ✉e-mail: liuhuan@genomics.cn; leil@mail.hzau.edu.cn; ningy@mail.hzau.edu.cn

(scRNA-seq) has been widely used in plant developmental biology[13,14]. Such studies provide insights into the roles and regulatory networks of different cell types during development. Single-cell transcriptome studies of maize shoot apical meristems, developing ears and roots have produced high-resolution maps of organ development and cell differentiation trajectories[15–17]. In these studies, intact tissues were first digested into protoplasts, which were then subjected to scRNA-seq. However, this procedure results in the loss of cell spatial information and therefore has several disadvantages: (1) not all cell types can be assigned to spatial locations by marker genes, (2) the same cell type could have different spatial locations and could differentiate into different tissues, and (3) the prediction of developmental trajectories based on single-cell sequencing remains challenging. These challenges are readily apparent in inflorescence primordia, which involve the sequential development of related meristem types.

Spatial heterogeneity is a key feature of tissue function and cell fate regulation. Recording transcriptional status with spatial coordinates is therefore necessary. The DNA nanoball (DNB)-based spatial transcriptome technology (spatial enhanced resolution omics-sequencing, or Stereo-seq) can analyse centimetre-scale samples with subcellular resolution and thus compensate for the shortcomings of single-cell sequencing[18]. Stereo-seq has been used for in situ capture of spatial transcriptomic information in animal models, such as the study of recovery in the salamander telencephalon following injury[19] and reconstructing the developmental trajectories of cell fate transitions and molecular changes during zebrafish embryogenesis[20]. However, spatial transcriptome sequencing has been performed successfully in a few types of plants, such as *Arabidopsis* leaves[21], peanut[22], tomato callus[23] and soybean nodule[24].

In the present study, we aimed to construct a high-resolution spatial transcriptional atlas of developing maize ears using Stereo-seq. This approach generated a valuable data resource for investigating gene expression, cell type organization and regulatory networks, ultimately enhancing our understanding of the mechanisms that underlie maize ear development and promoting yield improvement efforts.

Results

In situ RNA sequencing of developing maize ears by Stereo-seq

The architecture of the maize ear is determined during early development (~5–10 mm stage), when meristem initiation, maintenance and determinacy decisions start to form specific organs[6,25]. To generate a spatial transcriptome map of this critical developmental stage, we harvested ~6-mm-stage ear primordia of the B73 inbred line, which contained all meristem types (Fig. 1a). The ears were directly fixed in formalin–acetic acid–alcohol for 10 min and then quick-frozen in optimal cutting temperature resin, which ensures cell integrity and reduces the formation of damaging ice crystals (see Methods for details). Following a Stereo-seq protocol for plant tissues[21], 10-µm-thick frozen sections were attached to three 1 cm^2 chips for mRNA capture. Nucleic acid staining of cryosections was performed to check nuclear integrity (Fig. 1b). Intact sections were then used for Stereo-seq based on DNB sequencing technology[18]. The DNBs are precast to contain coordinate identities and unique molecular identifiers (UMIs) (Fig. 1b). We ultimately obtained high-quality spatial transcriptomes from four developing ear sections, with no transcript signal diffusion according to the UMI distribution (Supplementary Fig. 1).

Each DNB spot on the chip was 220 nm in diameter, and the centre-to-centre distance of two adjacent spots was 500 nm. After merging the high-resolution stained images and sequencing data in the Stereomics visualization system (https://www.stomics.tech/sap/), we compared the spatial clustering using different bin sizes, including bin20 (~10 µm, 20 × 20 DNB), bin50 (~25 µm, 50 × 50 DNB) and bin100 (~50 µm, 100 × 100 DNB). We found that bin50 produced a more accurate spatial clustering result (Supplementary Fig. 2). Therefore, bin50 (~25 µm) was chosen to represent each spot and construct the spatial transcriptome of developing ears. After removing low-quality bins (gene number < 150), we obtained a total of 34,559 bin50s from the four ear sections, with an average of 8,639 bin50s and 28,530 expressed genes per section (UMI counts greater than 1; Supplementary Table 1). The four sections shared similar gene and UMI numbers in each bin50, supporting the reproducibility of the Stereo-seq data (Supplementary Fig. 3). In summary, we generated high-quality in situ single-cell RNA sequencing datasets of developing maize ears by using Stereo-seq.

Spatial clustering and validation of cluster identities

We next pooled the bin50s of two adjacent sections, 1 and 2 (from the same ear), for unsupervised clustering analysis after imputation (for details, see Methods). A Uniform Manifold Approximation and Projection (UMAP) visualization revealed 12 distinct clusters (Fig. 1c). The spatial arrangement of eight cell types within the ear corroborated the previously published results[16]. Our Stereo-seq results also identified newly defined cell types. For example, we discovered three discrete cell types in the IM (Fig. 1d and Supplementary Figs. 4 and 5). These include IM tip (IMT), concentrated in the top four or five layers of the IM; IM periphery (IMP), along the outer periphery of the IM; and IM, in the central region of IM. The discovery of these distinct cell types highlights the complex tissue structure of maize ear primordia and holds substantial promise for delimiting discrete functional regions within the tissue landscape of the ear.

To verify the reliability of our Stereo-seq data, we next characterized the distribution of different cell types in two additional ear sections, 3 and 4. UMAP plots showed that bin50s from the two sections were classified into 11 and 13 clusters, respectively (Supplementary Fig. 6). Using the spatial information of the bin50s, we identified the physical location of each cluster (Supplementary Figs. 7 and 8). After comparing all four sections, we found that ten cell types (represented by bin50 clustering) could be repeatedly detected (in at least three sections). We used MetaNeighbor to determine how well the identity of bin50s in the stem cell types of one section could be predicted on the basis of their similarity to a cell type from another section, reported as the average area under the receiver operating characteristic curve (AUROC). Ten cell types with AUROC > 0.75 could be detected across at least two sections (Supplementary Fig. 9). We also identified a series of cluster-enriched genes and cluster-specific marker genes by analysing differentially expressed genes among these clusters. More than 70% of the marker genes showed the same spatial expression pattern in at least three sections (Supplementary Table 2), again supporting the reproducibility of our Stereo-seq data. To further validate the sensitivity and accuracy of the Stereo-seq method, we examined the expression patterns of 55 genes, including 24 well-characterized ear developmental genes selected from the literature[6–8,26–49] and 31 randomly selected marker genes identified by Stereo-seq, and we performed mRNA in situ hybridization experiments. This approach validated the spatial expression patterns of 74% of the genes (41/55; Supplementary Data 1). For example, in the Stereo-seq data, *3-ketoacyl-CoA synthase15* (*kcs15*) (Zm00001eb047970) and Zm*ZNF30* (Zm00001eb205550) were observed expressed specifically in the meristem epidermis (ME) and vasculature, respectively, in Stereo-seq, and these patterns were confirmed by mRNA in situ hybridization (Fig. 1e,f). Ultimately, all common cell types except the cortex and pith were verified by mRNA in situ hybridization. We also identified and validated four cell/domain types that have not been reported in previous studies[16], including those located in critical domains, such as meristem internal (corresponding to the cells of the meristem centre) as well as IMT, IMP and IM, as mentioned above. These results indicate that Stereo-seq can accurately portray the physical distributions of cell types and reveal specific gene expression patterns, and also enable the profiling of previously ungrouped meristem niche cell types that are hard to identify using traditional scRNA-seq.

https://doi.org/10.1038/s41477-024-01683-2

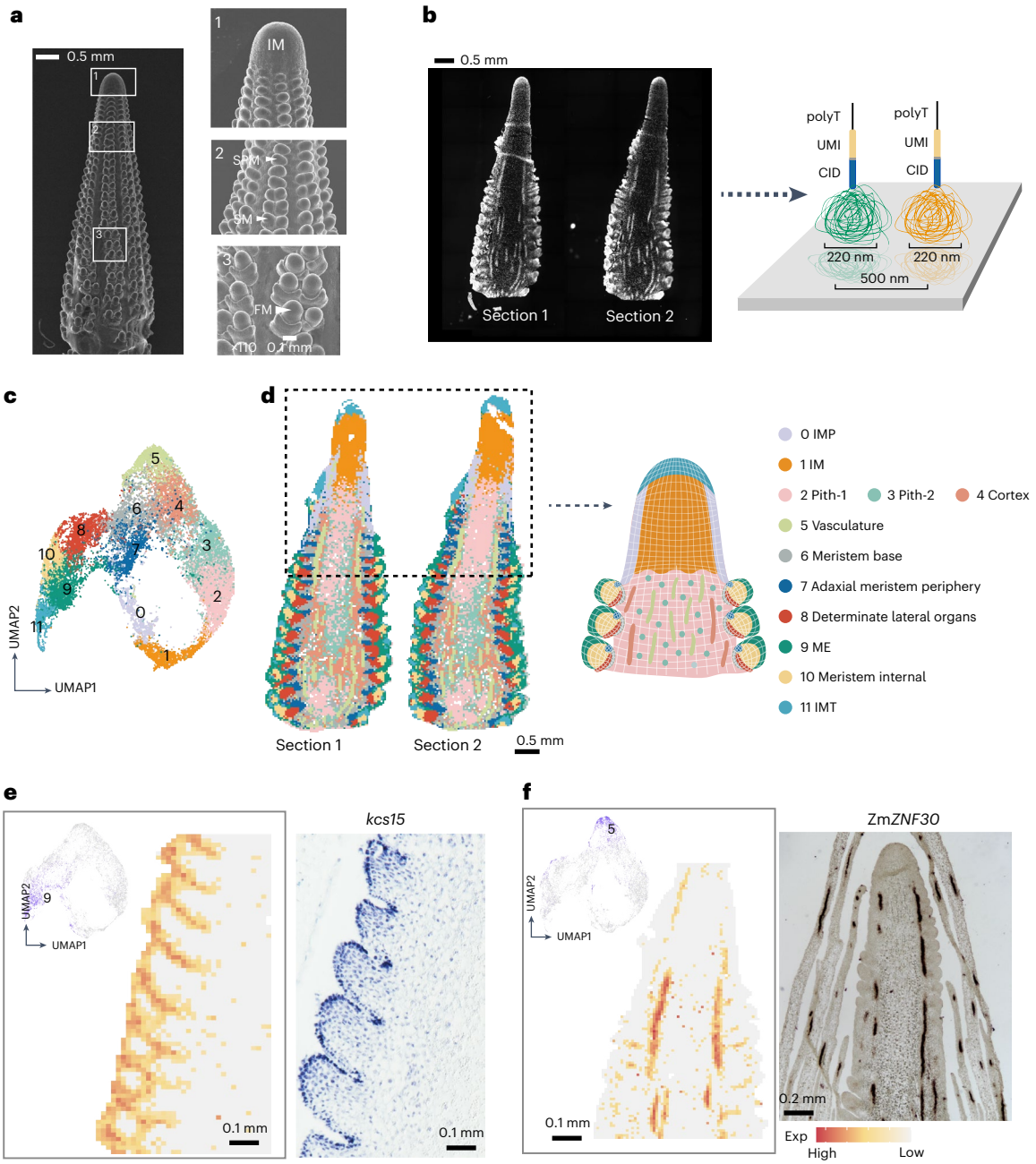

Fig. 1 | A spatial transcriptomic atlas of the developing maize ear. a, Left, a scanning electron microscope image of a developing maize ear. Right, close-ups of the IM, spikelet pair meristems (SPM), spikelet meristems (SM) and floral meristems (FM). **b**, Left, nucleic acid dye staining of 6 mm developing maize ear sections attached to a 1 cm^2 chip. Right, diagram of the Stereo-seq process, showing the size of each spot and the distance between two adjacent spots. CID, coordinate identity. **c**, Twelve clusters are displayed in an integrated UMAP plot in two dimensions. Each dot represents a bin50 from sections 1 and 2. **d**, Left, spatial distribution of cell types that were identified in sections 1 and 2: IMP, IM, vasculature (including xylem, phloem and bundle sheath), meristem base, adaxial meristem periphery, determinate lateral organs, ME, meristem internal and IMT. Right, schematic of a 6 mm maize ear showing the cell identities detected by Stereo-seq. **e**, mRNA in situ hybridization of kcs15 (right) validates Stereo-seq cluster 9, the ME (left). **f**, mRNA in situ hybridization of ZmZNF30 (Zinc Finger Protein 30, right) validates Stereo-seq cluster 5, the vasculature (left). Zm*ZNF30* was also validated as marker gene for phloem16. The experiments in **a**,**e**,**f** were repeated in at least three independent sections. In **b**, Stereo-seq was applied in two independent sections (sections 1 and 2). In **f**, Exp present gene expression level.

Two MADS-box genes identified through Stereo-seq contribute to stem cell differentiation

We next asked whether the Stereo-seq dataset could advance our understanding of how stem cell determinacy shifts from the indeterminate IM to the more determinate spikelet and floral meristems. Since these different meristem types are highly similar, traditional scRNA-seq strategies cannot distinguish their spatial positions and expression profiles[16]. By contrast, our spatial transcriptome map could distinguish different meristem types by segmenting their physical locations. Therefore, on the basis of their spatial position, we extracted the bin50s of indeterminate and determinate meristems from IM, spikelet meristem and floral meristem. A total of 1,182 bin50s from section 1 (determinate ME = 837, IMT = 345), 1,394 bin50s from section 2 (ME = 970, IMT = 424), 674 bin50s from section 3 (ME = 589, IMT = 85) and 765 bin50s from

section 4 (ME = 666, IMT = 99) were obtained and re-clustered. This generated three sub-clusters (Fig. 2a and Supplementary Fig. 10), which were clearly distributed in distinct developmental domains, including the indeterminate IMT, determinate spikelet/floral meristem periphery and determinate spikelet/floral meristem tip. These results indicate that our re-clustering could separate highly similar stem cell types, enabling us to investigate the changes in gene expression that govern stem cell fate during ear development.

We next performed a comparative analysis to identify the possible regulators that control stem cell determinacy. A series of differentially expressed genes among the three sub-clusters were detected using the Seurat FindAllMarkers function (Supplementary Table 3; min.pct, 0.3; fold change, >2; padj, <0.01)[50]. These included two MADS-box genes, Zm*MADS8* and its paralogue Zm*MADS14* (Fig. 2b and Supplementary Fig. 10), with specific expression in determinate spikelet/floral meristem tips in Stereo-seq, and their expression patterns were validated by mRNA in situ hybridization (Fig. 2c,d and Supplementary Fig. 11). A previous study suggested that misexpressing Zm*MADS8* and *DROOPING LEAF2* in the meristem could activate a leaf program, changing meristem identity to produce a branch[51,52], thus implying a function for Zm*MADS8* in stem cell determinacy. To test this, we generated double knock-out mutants of Zm*MADS8* and *14* using CRISPR–Cas9 genome editing (Supplementary Fig. 12). The single mutants developed normally, producing normal spikelets and fertile florets. Similarly, the *CR*-Zm*mads8/14* double mutants developed normally, including their inflorescence and spikelet meristems (Supplementary Fig. 13). However, the double-mutant floral meristems were converted to indeterminate ear branches. This indicates that Zm*MADS8* and *14* are key regulators that impose floret identity on stem cells (Fig. 2e–p). In summary, our results indicate that Zm*MADS8* and Zm*MADS14* redundantly play a critical function in programming the differentiation of pluripotent stem cells into determinate floral meristems during maize ear development. The spatial transcriptome generated by Stereo-seq thus provides new insights into crop inflorescence development and facilitates the identification of key developmental regulators.

Two major trajectories in developing maize ears

We next established a developmental trajectory for the developing ear predicated on its anatomical framework. Employing Monocle2 (ref. 53) for pseudotime analysis, we found that bin50s originating from the IMT appeared early along the pseudotime trajectory (Fig. 3a,b). This suggests that the IMT cells are less differentiated than other cell types; thus, IMT cells are more likely to be the origin of the trajectory. Subsequently, in the early pseudotime stages, bin50s were predominantly localized in the regions of the ME, MI and meristem base. As the pseudotime progressed to middle and later stages, bin50s were primarily situated in the pith, cortex and vasculature (Supplementary Fig. 14). This distribution pattern suggests a distinct differentiation state between the spikelet meristem and the vascular bundle.

To validate this cellular differentiation trajectory, we performed an RNA velocity analysis, which revealed two primary trajectories traced along the pseudotime continuum (Fig. 3c and Supplementary Fig. 15): (1) bin50s localized in the ME undergoing differentiation towards the meristem base and (2) bin50s in the upper region of the vasculature undergoing differentiation towards the primordium base. These observations suggest no fewer than two developmental trajectories in the maize ear. Specifically, the spikelet meristem trajectory is marked by vertical differentiation, whereas the vascular bundle trajectory is indicative of horizontal expansion processes (Fig. 3d).

Construction of spatial regulatory networks by integrated analysis of scRNA-seq and Stereo-seq

Our findings from spatial clustering (Fig. 1) and trajectory analysis (Fig. 3) were consistent with the expected developmental processes of the maize ear, suggesting that our spatial transcriptome dataset could provide valuable clues to understanding the gene expression patterns at the cell-type level. However, despite the effectiveness of spatial transcriptomics in identifying the physical distributions of cell types, it does not operate at the single-cell level. To obtain additional information at a single-cell level, we used scRNA-seq to construct a more detailed transcriptome map. The enzymatic dissociation of cells during protoplasting results in a loss of spatial information. A combination of scRNA-seq and spatial transcriptomics could therefore improve the resolution of cell types and reveal their functional characteristics. We performed scRNA-seq using ear primordia at the same developmental time point as those used for Stereo-seq (~6–8 mm stage). Protoplast suspensions from two independent replicates were made into libraries and sequenced, with comparable UMIs and detected gene numbers (Methods, Supplementary Figs. 16 and 17a, and Supplementary Table 1). After removing protoplasting-induced genes[16] and filtering low-quality cells with >5% mitochondrial transcripts and <1,500 expressed genes, we obtained 14,243 cells and 28,627 expressed genes (with UMI > 1).

Before performing unsupervised analysis, we removed batch effects between the two replicates using the Harmony algorithm (Supplementary Fig. 17b)[54]. We then visualized clustering using a UMAP plot, which grouped the cells into 13 clusters (Fig. 4a). To introduce spatial information to the scRNA-seq clusters (Sc-Clusters), we integrated the scRNA-seq and Stereo-seq data by applying STRIDE[55] to calculate the proportion of cells (from scRNA-seq) in each bin50. The STRIDE prediction results revealed that cells of Sc-Clusters 0, 3 and 4 were from the IM, while cells of Sc-Clusters 1, 11 and 12 were mainly from the vasculature, meristem internal and ME, respectively (Fig. 4b and Supplementary Fig. 18). The same conclusions could be drawn using bin50s from sections 3 and 4 (Supplementary Figs. 19 and 20). To further verify the accuracy of our integration results, we identified 2,864 genes as cluster-specific markers in scRNA-seq (Supplementary Table 4; min.pct, 0.3; log2fc.threshold, 0.25; padj, <0.01) using the Seurat FindAllMarkers function and verified their expression patterns in the Stereo-seq data (Fig. 4c). Except for Sc-Cluster 11, at least five genes provide support for the prediction of the spatial information for each Sc-Cluster (Supplementary Figs. 21–23), demonstrating the reliability of STRIDE for the integration of scRNA-seq and Stereo-seq data.

To understand gene regulation in developing ears, we next built co-expression networks using the scRNA-seq datasets with WGCNA[56]. We identified 12 gene modules whose constituent genes were expressed in a highly coordinated manner (Supplementary Fig. 24 and Supplementary Table 5). For example, 40.2% of the genes in module 3 exhibited the highest expression level in the vasculature (Sc-Cluster 1). Module 3 genes were involved in the phenylpropanoid metabolic process (GO:0009699; Supplementary Fig. 25a) and phenylpropanoid biosynthesis pathway (KEGG:00940), which serves as the initial step of lignin biosynthesis[57,58]. The vasculature includes xylem tissues with several lignified cell types, such as vessel elements (which transport water) and tracheid fibres. In module 5, 76.9% of the genes had the highest expression levels in IM cells (Sc-Cluster 4), and GO enrichment revealed that module 5 genes were enriched in carbon metabolism pathways, such as organic acid catabolic process activity (GO:0016054; Supplementary Fig. 25b). In module 7, 86.7% of the genes had the highest expression level in ME cells (Sc-Cluster 12), and these genes were significantly enriched in processes related to fatty acid metabolism (GO:0006633) and the biosynthesis of cutin and wax (GO:0010025; Supplementary Fig. 25c). The plant cuticle, composed of a lipophilic layer of cutin and cuticular waxes, covers the surface of the epidermis and plays a crucial role in limiting non-stomatal water loss, facilitating gas exchange, and providing mechanical strength and viscoelastic properties[59]. Together, these results suggest that genes within the same module probably function in the same cell types and are associated with region-specific biological functions of cells.

To explore the core regulatory genes in each of these cell types, we next exported gene modules to Cytoscape[60] to construct

https://doi.org/10.1038/s41477-024-01683-2

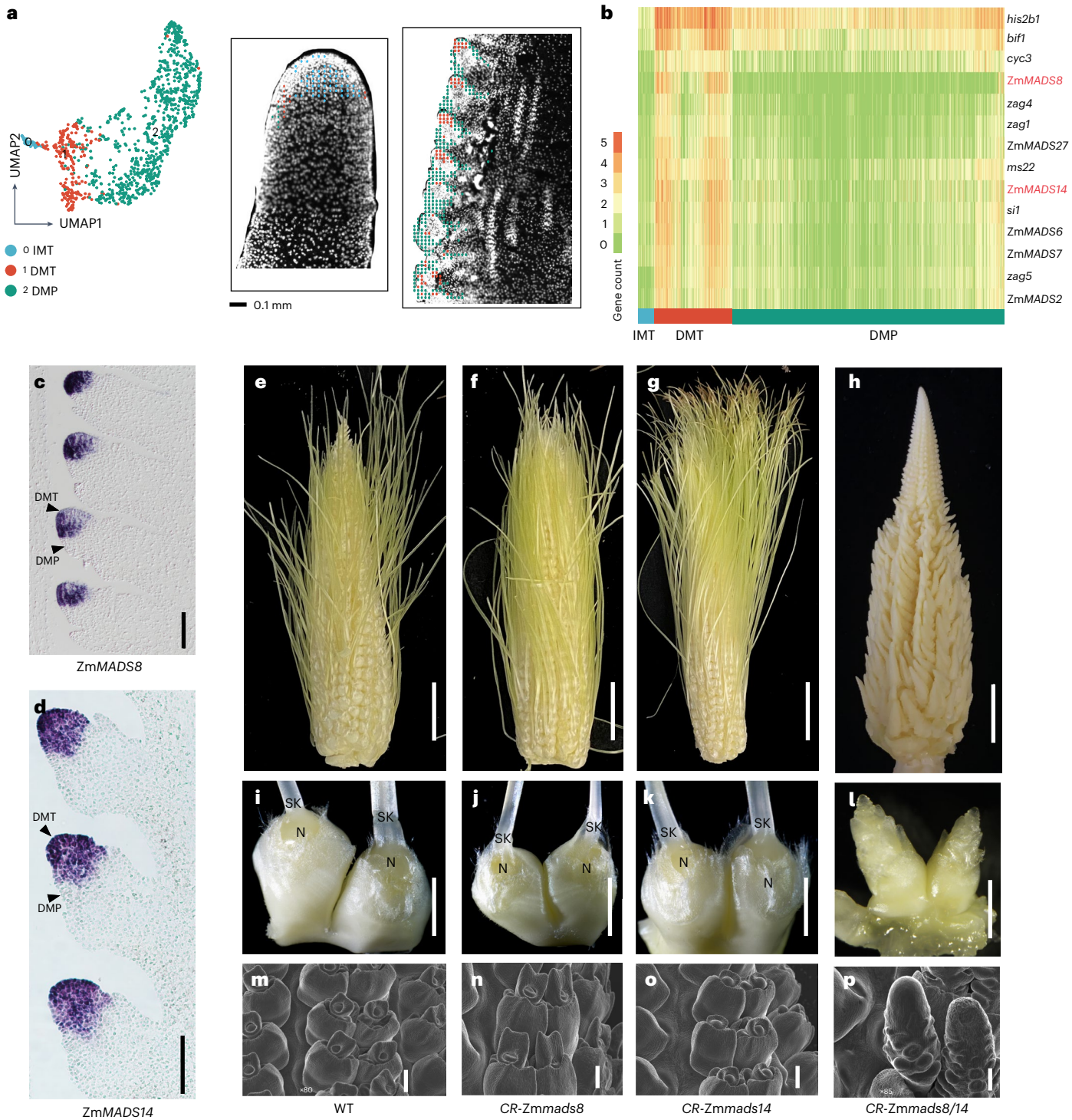

Fig. 2 | Zm*MADS8* and Zm*MADS14* identified using Stereo-seq data contribute to stem cell differentiation. a, Left, Stereo-seq enables the extraction of bin50s distributed in the ME and the IMT. The UMAP plot reveals the presence of three sub-clusters. Right, physical distribution of bin50s of three sub-clusters on section 1. Stereo-seq was applied in one independent section (section 1). DMT, determinate meristem tip; DMP, determinate meristem periphery. **b**, Heat map showing the mean expression levels of the 14 genes involved in maize ear development that are highly expressed in the DMT. Zm*MADS8* and Zm*MADS14* are highlighted in red. **c**,**d**, mRNA in situ hybridization with antisense probes of Zm*MADS8* (**c**) and Zm*MADS14* (**d**). The arrowheads point to the DMT and DMP. These experiments were repeated in at least three independent sections. Scale bars, 0.1 mm. **e**–**h**, The ear phenotypes of the wild type (WT) (**e**), *CR*-Zm*mads8* (**f**), *CR*-Zm*mads14* (**g**) and *CR*-Zm*mads8/14* (**h**), with the latter showing the conversion to branches. Scale bars, 2 cm. **i**–**l**, The female floret phenotypes of the wild type (**i**), *CR*-Zm*mads8* (**j**) and *CR*-Zm*mads14* (**k**) and the conversion to branches in *CR*-Zm*mads8/14* (**l**). SK, silk; N, nucellus. Scale bars, 0.5 cm. **m**–**p**, Scanning electron microscope images of the floret meristem in the wild type (**m**), *CR*-Zm*mads8* (**n**) and *CR*-Zm*mads14* (**o**) and the conversion to branches in *CR*-Zm*mads8/14* (**p**). Scale bars, 0.2 mm. The experiments in **e**–**p** were repeated in at least three independent ears.

https://doi.org/10.1038/s41477-024-01683-2

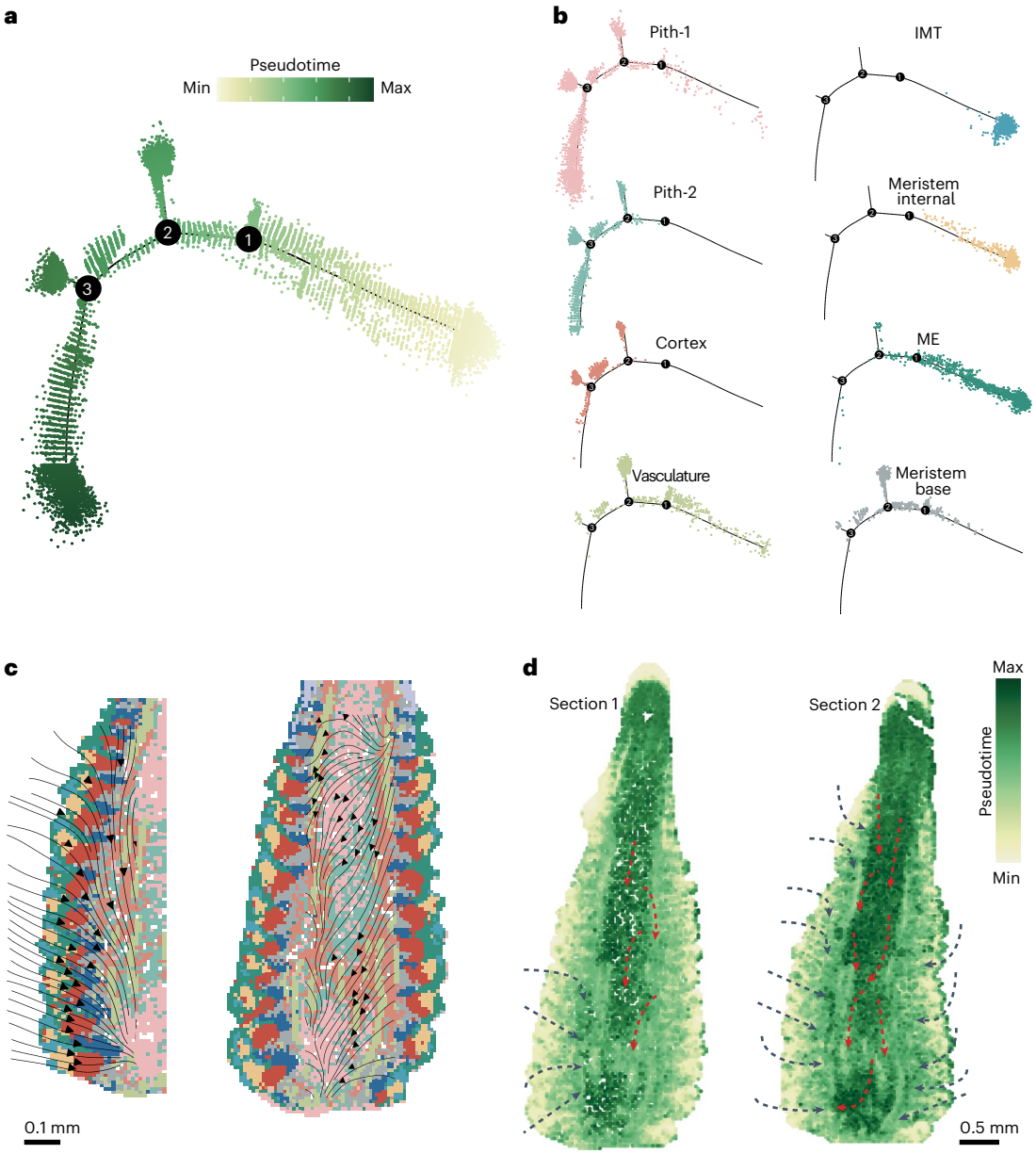

Fig. 3 | Developmental trajectories of the 6 mm maize ear. a, Pseudotime analysis using bin50s of sections 1 and 2. **b**, Distribution of bin50s located mainly in the spikelet meristems and vascular bundles on the pseudotime trajectory branches. **c**, RNA velocity streamline plots showing the predicted trajectories of bin50 transitions in the spikelet meristems and the vascular bundles. **d**, RNA velocity analysis showing the predicted trajectory of the 6 mm maize ear. bin50s are coloured according to their vector-field-based pseudotime score and positioned in the same coordinates as in Fig. 1d. The black arrows show the differentiation trajectory in the spikelet meristems (vertical differentiation), and the red arrows show the differentiation trajectory in the vascular bundles (horizontal expansion).

a co-expression network. The connectivity of each gene was calculated by summing its connection strengths with other genes. Some nodes were considered to be hub genes, since their expression pattern correlated with numerous genes (with a higher number of directed edges and neighbourhood connectivity; Supplementary Fig. 26). The biological functions of these hub genes also showed that they probably contributed to the development of the cell types in which they were expressed. For example, *OUTER CELL LAYER* (*OCL*) genes function in cuticle biosynthesis in *Arabidopsis* and maize[61–63]. In module 7, we identified *OCL5* (Zm00001eb171720) as a hub gene with the highest connection to multiple *kcs* and *GLOSSY* genes (Fig. 4d), which are known to participate in wax and cutin biosynthesis[64,65]. Furthermore, Stereo-seq data indicated that *OCL5* was specifically expressed in the ME (Fig. 4g), consistent with the notion that the cuticle synthesis process is regulated by *OCL*, *kcs* and *GLOSSY* genes occurring in these cells.

We also found that multiple laccase genes were enriched in module3 (*laccase9* (Zm00001eb149240), *laccase7* (Zm00001eb147860), *laccase14* (Zm00001eb127360), *laccase11* (Zm00001eb012250) and *laccase2* (Zm00001eb289630)). Laccase genes are implicated in lignin biosynthesis in *Arabidopsis*[66,67], suggesting that they act similarly to promote vessel development in maize. *Peroxidase19* (Zm00001eb131000) and *peroxidase5* (Zm00001eb282430) had the highest connectivity to laccase genes (Fig. 4e), and Stereo-seq data indicated that *peroxidase19* was specifically expressed in the vessels (Fig. 4g). Peroxidase enzymes transfer monolignols to lignin, and we therefore speculate that peroxidase and laccase genes together regulate lignin composition.

https://doi.org/10.1038/s41477-024-01683-2

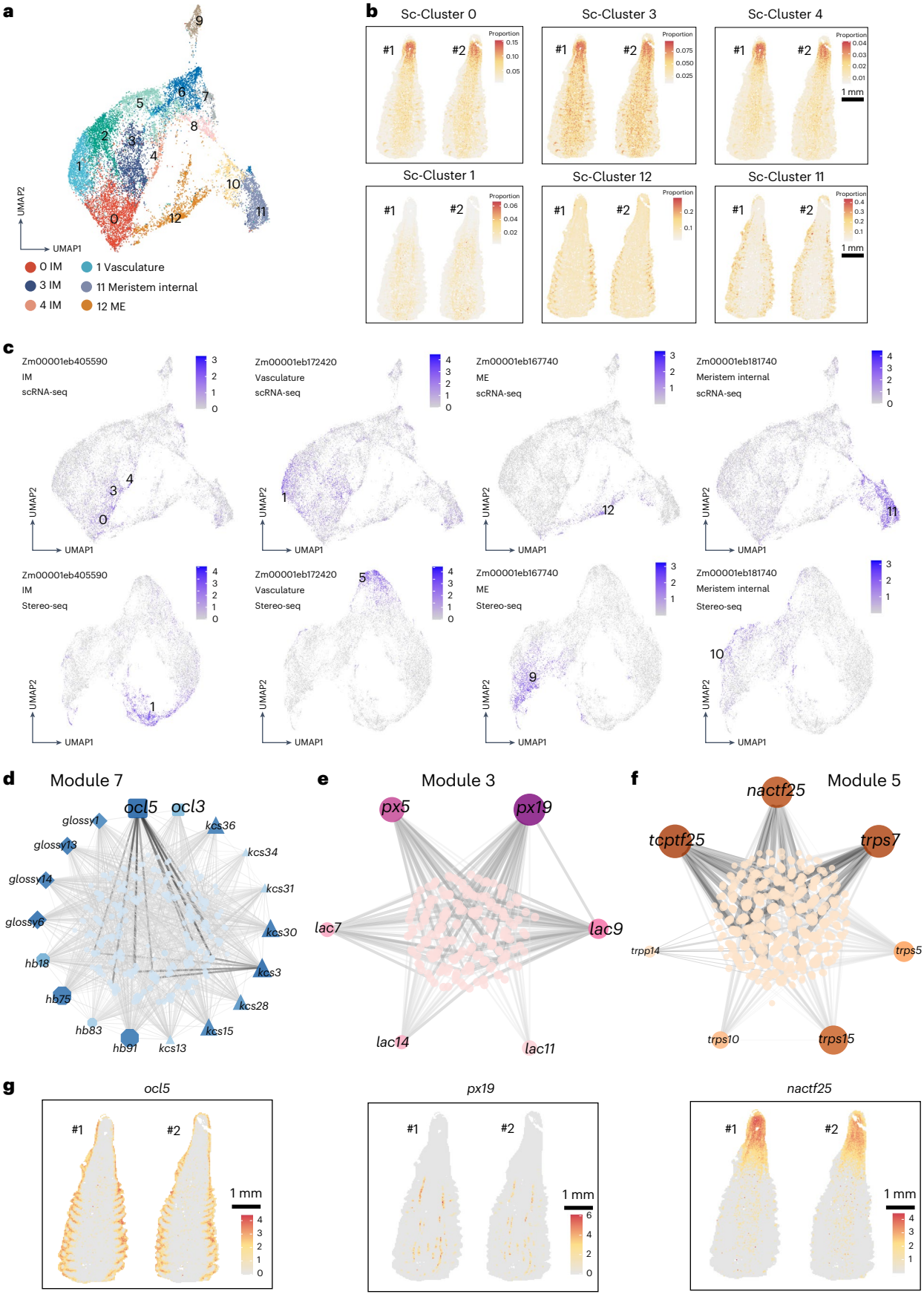

Fig. 4 | Construction of spatial co-expression networks by integrating scRNA-seq and Stereo-seq data. a, Thirteen clusters visualized by an integrated UMAP plot in two replications. Each dot represents a cell. **b**, The proportions of cells from different Sc-Clusters on sections 1 and 2 (#1 and #2). **c**, Top, UMAP plots of marker genes from the scRNA-seq data. The numbers in the plots indicate that the gene is the marker gene of the corresponding Sc-Cluster, and the colour scale indicates the normalized expression level in the scRNA-seq data. Bottom, UMAP plots of the same genes from the Stereo-seq data. The numbers in the plots indicate that the gene is the marker gene of the corresponding cluster, and the colour scale indicates the normalized expression level in the Stereo-seq data from sections 1 and 2. **d**–**f**, Co-expression networks of genes in modules 7 (**d**), 3 (**e**) and 5 (**f**). The networks were visualized with Cytoscape. Node size represents the relative connectivity. The line shade represents the weight of the edge between two nodes. **g**, Spatial visualization of three hub genes from modules 3, 5 and 7 on sections 1 and 2. The colour scale indicates the normalized expression level.

We next identified that module 5 was abundant in genes related to trehalose synthesis, including a trehalose-6-phosphate phosphatase (*trpp14*, Zm00001eb018720) and four trehalose-6-phosphate synthase genes (*trps7*, Zm00001eb153280; *trps15*, Zm00001eb370990; *trps5*, Zm00001eb098910; and *trps10*, Zm00001eb192680). Trehalose-6-phosphate is a key signal in plant development, and overexpression of *TRPP* genes in maize ears increased kernel set and harvest index under drought stress[68,69]. A NAC transcription factor (Zm00001eb405590, also annotated as *NACTF25*), served as a hub gene with high connection to these genes (Fig. 4f). Meanwhile, our Stereo-seq data showed that *NACTF25* was strongly expressed in the IM (Fig. 4g). Although *NACTF25* has not been reported to contribute to maize ear development, NAC transcription factors directly regulate the expression of *TRPP* genes and influence yield in rice[70]. We therefore predict that *NACTF25* might affect IM growth by regulating multiple *TRPP* and *TRPS* genes.

To further investigate whether hub genes in our expression network might contribute to maize yield, we estimated the narrow-sense heritability (h^2) of ear morphology traits related to yield[71,72]. We queried a phenotyped association mapping panel of 507 maize lines for hub genes that were highly expressed in the vasculature (module 3), IM (module 5) and ME (module 7), comparing them with a distribution of h^2 estimates from random subsets of genes (expressed higher than the hub genes' average expression level). Using single nucleotide polymorphisms (SNPs) within 2 kb of genes[73], we found that hub genes that were highly expressed in the vasculature (module 3) and IM (module 5) had greater SNP heritability than the 95th percentile of random genes for cob diameter, kernel row number and ear length traits. In addition, hub genes that were highly expressed in the ME (module 7) had greater SNP heritability than the 95th percentile of random genes for kernel number per row (Supplementary Fig. 27 and Supplementary Table 6). In summary, our findings demonstrate the benefits of integrating single-cell and spatial transcriptome data and highlight the power of this method in identifying candidate genes associated with maize yield-related traits.

Discussion

The maize ear is an excellent model to study meristem fate transitions during development, with the potential to optimize morphology to enhance grain yield[74–76]. Many spatiotemporally expressed genes act early in development to determine ear size and kernel number of the maize ears, requiring us to understand gene expression at the spatial and single-cell levels. A previous study generated a single-cell-resolution map of the developing maize ear primordium using scRNA-seq data from protoplasts, demonstrating that these data could facilitate genetic studies[16]. However, limited by the number and resolution of marker genes, the molecular definitions and spatial information of cell types are largely incomplete and difficult to identify in plants. Stereo-seq is a recently developed DNB-based spatial transcriptome technology that has been applied to animal models[18–20] and *Arabidopsis* leaves[21]. This method enabled us to generate a more precise spatial transcriptome profile of the maize ear and to clearly distinguish 12 cell types (sections 1 and 2). Ultimately, 8 of these 12 cell types were consistent with a previous scRNA-seq study. Four newly defined cell types in our study were also supported by mRNA in situ hybridization evidence, including IM, IMP, IMT and meristem internal. These findings will substantially enhance our understanding of cell types in the developing maize ear and their respective biological functions.

On the basis of our high-resolution Stereo-seq data, we found that two major trajectories initiated from the IMT. Taking advantage of our spatial transcriptome, we extracted and re-clustered indeterminate and determinate meristem components from the IM, spikelet meristem and floral meristem. Because of their similarity, these meristem cells could not be resolved by scRNA-seq analysis[16]. We found that two paralogues, Zm*MADS8* and Zm*MADS14*, were specifically expressed in the determinate spikelet/floral meristem tips and controlled floral stem cell determinacy. The Stereo-seq spatial transcriptome therefore provides new insights into maize inflorescence development and facilitates the identification of key regulators underlying specific developmental processes that could inform crop yield improvement.

By employing a deconvolution algorithm to evaluate the similarity between scRNA-seq and spatial transcriptome data, we inferred the identities of six clusters and validated three spatially resolved gene modules in scRNA-seq. Furthermore, we found that the hub genes in the core co-expression networks were closely related to the biological functions of their cell types/tissues. Modifying such hub genes could offer a new solution to avoid gene redundancy in breeding strategies. For example, the hub gene *NACTF25* was co-expressed with a cluster of *TRPP* and *TRPS* genes, which function in the synthesis of trehalose-6-phosphate. Members of these gene families regulate maize ear development[77]. Follow-up studies could test whether *NACTF25* could be used to overcome the redundancy of the *TRPP* gene family in future breeding strategies. Our results highlight the advantages of Stereo-seq for constructing a comprehensive and precise spatial transcriptome map of the maize ear. In addition, Stereo-seq can be successfully used to infer the cell type identities from standard scRNA-seq studies. In the near future, as Stereo-seq continues to evolve and enhance its capacity for in situ mRNA capture, the integration of spatial and single-cell transcriptomics will also become more precise and efficient.

In summary, the implementation of Stereo-seq technology in our study has proved to be a powerful tool for obtaining a comprehensive spatial transcriptome map of the developing maize ear. The data generated using this approach not only serve as a valuable genetic resource but also provide insights into the development of the maize ear at a higher resolution. The knowledge gained here can inform the process of maize yield improvement and deepen our understanding of IM development. Our exploration of the application of Stereo-seq methodology in this context contributes valuable experience to the field of plant spatial transcriptomics, paving the way for future advancements in this area.

Methods

Plant growth conditions and tissue fixation

Maize B73 inbred plants were grown in the field (April–July) at Huazhong Agricultural University in Wuhan, Hubei, or in a greenhouse with 12 hours of daylight at temperatures ranging from 26 to 28 °C during the day and 22 to 24 °C at night. Developing ears (~6 mm) were collected at the 11- or 12-leaf stage and immediately fixed in a 50% formalin–acetic acid–alcohol solution (50% absolute ethanol, 10% formaldehyde, 5% acetic acid, v/v/v) for 10 min. The tissues were then treated with 2% sucrose solution (1 PBS buffer, pH 7.4, 2% sucrose, v/m) and vacuumed on ice for 15 min each; then, the solution was changed and

vacuum applied for an additional 15 min. The ears were then embedded in pre-chilled optimal cutting temperature resin (Sakura), snap-frozen in liquid nitrogen pre-chilled isopentane for 10 s and stored at −80 °C for later use.

The maize double-mutant *CR*-Zm*mads8/14* transgenic lines were generated in the KN5855 genetic background. The mutations were detected by PCR with the primers listed in Supplementary Table 7. The *CR*-Zm*mads8/14* double mutants were crossed with the wild type and then self-crossed to segregate the *CR*-Zm*mads8* and *CR*-Zm*mads14* single mutants, which were evaluated in the field in two environments: summer 2020 in Wuhan (30° N, 114° E) and spring 2021 in Sanya (18.34° N, 109.62° E), China. The scanning electron microscope observations of ears were performed at the seven- to eight-leaf stage.

Scanning electron microscope observations

Immature ears (~5–6 mm) of B73, KN5585, *CR*-Zm*mads8*, *CR*-Zm*mads14* and *CR*-Zm*mads8/14* were collected from plants at the seven- to eight-leaf stage grown in the field at Huazhong Agricultural University in Wuhan, Hubei, or in a greenhouse maintained at 26–28 °C during the day and 22–24 °C at night with a 12-hour light–dark cycle. The husk leaf primordia were quickly removed, and the bracts and the ears were observed using a Jeol JSM-7900F scanning electron microscope, as previously described[44].

Nucleic acid staining

For nucleic acid staining, 10 µm slices of the sample were placed on a sticky slide (ProbeOn Plus, Fisher) and dewaxed with 100% Histoclear (10 min) twice, followed by an alcohol gradient (100% to 95% to 85% to 70% to 50% to 30% to ddH_2O) for 2 min each time. The slides were then placed in 1× PBS buffer for 2 min, and finally the sections were stained with 0.1 µg ml^{-1} DAPI. After staining for 3–5 min, the slides were rinsed with 1× PBS buffer. After rinsing, the slides were covered and observed under a fluorescence microscope.

In situ hybridization

Immature maize B73 ears, measuring 5–6 mm in length, were fixed in a 4% PFA solution (4 g of paraformaldehyde (Sigma-Aldrich) dissolved in 100 ml of 1× PBS, pH 6.5–7). The ears were dehydrated in a series of ethanol concentrations and cleared in Histoclear, embedded in Paraplast Plus (Sigma, P3683) and sectioned to a thickness of 8 µm. To generate sense and antisense RNA probes, probe fragments were amplified by PCR using the primers listed in Supplementary Table 7. A sequence (CATTAATACGACTCACTATAGGG) was incorporated in the 5′ or 3′ primers for sense and antisense RNA probes, respectively. The probes were then transcribed in vitro using T7 RNA polymerase[28] and labelled with digoxigenin-UTP[28]. Finally, RNA hybridization, immunologic detection and signal capture of the hybridized probes were performed as previously described[4].

Stereo-seq library preparation and sequencing

The experimental method was based on the previously reported Stereo-seq standard protocol v.1.1 with some modifications[18]. The embedded developing ear tissues were sectioned longitudinally at 10 µm thickness (Leica, CM1950). Tissue sections were adhered to the Stereo-seq chip surface and incubated at 37 °C for 2 min. The tissues were then fixed in methanol and incubated at −20 °C for 40 min, treated with a nucleic acid dye stain (Thermo Fisher, Q10212) for 5 min and observed under a microscope to ensure the integrity of the nuclei (unfrozen 6 mm ear sections were used as a control (Supplementary Fig. 28)). The same sections were also used for bright-field imaging, and both types of images were taken with a Motic PA53 Scanner. Tissue sections were de-crosslinked in TE buffer (10 µM Tris, 1 µM EDTA, pH 8.0) at 55 °C for 1 hour. The sections were then permeabilized at 37 °C for 12 min and incubated overnight at 42 °C for reverse transcription and complementary DNA synthesis. Afterwards, the tissue was digested at 37 °C for 30 min and treated with Exonuclease I (NEB, M0293L) for 1 hour at 37 °C. The cDNA products were purified using Ampure XP Beads (Vazyme, N411-03) (0.6× and 0.15×), used for DNB generation and finally sequenced (paired-end 50 bp or paired-end 100 bp) on an MGI DNBSEQ-Tx sequencer.

Raw Stereo-seq data processing and quality control

Stereo-seq raw reads were generated from an MGI DNBSEQ-T5 sequencer. Read 1 contained coordinate identity and UMI sequences (coordinate identity, 1–25 bp; UMI, 26–35 bp), while read 2 contained the cDNA sequence. Retained reads were then aligned to the reference genome B73 (ref. 78) via STAR[79], and mapped reads with MAPQ10 were counted and annotated to their corresponding genes using an in-house script (available at https://github.com/BGIResearch/handleBam). A gene-location expression matrix containing location information was then generated.

Binning data of spatial Stereo-seq

After obtaining the raw spatial data, we merged the transcripts captured by 50 × 50 DNBs into one bin50. We treated the bin50 as the fundamental analysis unit, and bin IDs were composed of *X* and *Y* coordinates on the capture chip. The threshold for filtering low-quality bins was set to <150 or >5,000 gene counts. After filtering, the remaining bin50s were included in the downstream analysis (the details are provided in Supplementary Table 1).

Recovering missing values and unsupervised clustering of Stereo-seq data

The raw gene–bin50 matrices were loaded into the Seurat package (v.4.1.1)[50], which was implemented in R (v.4.3.1) (https://cran.r-project.org/). We then performed normalization in the origin dataset (LogNormalize, scaling factor 10,000), using the FindVariableFeatures function (vst method, 2,000 features) to identify highly variable genes; scaled the data with the ScaleData function; performed principal component analysis (PCA) with the RunPCA function (100 principal components); and determined the statistical significance of the PCA scores with the JackStraw function. Clusters were identified using the Seurat function FindClusters with a resolution of 1. The data structures were separately visualized and explored by UMAP (the RunUMAP function was run with the following settings: dims, 15; metric, correlation; min.dist, 0.01). However, many genes were expressed in only a subset of bin50s (Supplementary Fig. 29). We therefore used the Seurat Wrapper function RunALRA[80,81] to impute missing expression values, increasing the non-zero percentage of expressed genes from 3.0% to 66.4% in sections 1 and 2, from 3.8% to 62.9% in section 3 and from 3.1% to 72.6% in section 4 (Supplementary Fig. 29). After obtaining the imputed cell–bin50 matrices, we performed the downstream analyses as previously described. Briefly, we detected variable genes with the FindVariableGenes function (vst method, 2,000 features), scaled data with the ScaleData function, performed PCA with the RunPCA function, clustered bin50s with the Louvain method (FindNeighbors and FindClusters) and visualized the data with nonlinear dimensional reduction algorithms (RunUMAP). The physical distribution of cell types before and after imputation was consistent (Supplementary Fig. 30). More importantly, the clustering of imputed datasets showed more clear anatomical characteristics in some regions, especially in the meristems and vasculature (Fig. 1d).

Identifying cluster marker genes of clusters in the Stereo-seq and scRNA-seq data

Cluster-enriched genes were identified with the FindMarkers function of the R package Seurat[50]. Two-sided Wilcoxon rank-sum tests were used to identify genes with significant expression differences between different cell clusters, with the parameters log2fc.threshold, 0.25; p_val_adj, <0.01. The following thresholds were used to identify

cluster-specific marker genes: the $\log_2$ (fold change) of genes was >0.25, and the proportion of marker genes expressed in cells among corresponding clusters was >30%.

MetaNeighbor analysis

MetaNeighbor analysis was performed using the R function MetaNeighbor (v.1.20.0) with the default settings[82]. The AUROC scores produced by the MetaNeighbor analysis indicate the degree of correlation between cell groups.

Monocle 2 analysis

Pseudotime trajectories were reconstructed using Monocle2 (v.2.22.0)[53]. The count matrix was first converted to a CellDataSet object. Differentially expressed genes were then identified using the FindAllMarkers function in the R package Seurat (min.pct, 0.5; log2fc.threshold, 1) and filtered by p_val_adj < 0.01. Dimensional reduction clustering and pseudotime trajectory inference were performed using the reduceDimension function and the orderCells function, respectively, with the default parameters.

RNA velocity analysis

We classified genes into three types—unspliced, spliced and ambiguous—using the CIGAR alignment information in the BAM file, as previously described[83]. To further preprocess the data, we scaled the spatial position of the sections on the chips and removed invalid reads and alignment results located on the periphery of the section. The preprocessed BAM file was then used to generate a sparse matrix, which was subsequently converted to an adata format using the R package anndata[84] (https://github.com/theislab/anndata). The entire process could also be performed using a local script (https://github.com/wjwei-handsome/bam2adata).

We performed data normalization and clustering using the default parameters of the scanpy[84] and scvelo[85] packages. Highly variable genes were selected as feature genes, and dimensionality reduction was performed via UMAP. Subsequently, kinetic parameters and gene-wise RNA velocity vectors were estimated on the normalized matrix and projected onto the visualized spatial plot to retain spatial information. We used streamlines to visualize the velocity vector flows on the 6 mm maize ear section.

Unsupervised clustering of indeterminate and determinate meristems

After obtaining the unsupervised clustering of the Stereo-seq data, we extracted the bin50s from the ME and IMT in the four sections. The new gene–bin50 matrices were loaded into the Seurat package, and the downstream analyses were performed as described above. Clusters were identified using the Seurat function FindClusters with a resolution of 0.2. The data structures were separately visualized and explored by UMAP (we ran the RunUMAP function with the following settings: dims, 10; metric, correlation; min.dist, 0.01).

Protoplast preparation

Protoplasts were prepared as described previously[86,87]. In brief, approximately thirty 6 mm developing ears were dissected with sharp razor blades into 0.5–1 mm slices in 0.4 M D-mannitol. After discarding the mannitol, we immediately transferred the slices into a 35 mm Petri dish containing 4 ml of enzyme solution, consisting of 0.6 M D-mannitol, 1% (w/v) Cellulase Onozuka R-10 (Research Products International), 0.2% (w/v) Macerozyme R-10 (Research Products International), 20 mM 2-(*N*-morpholino)ethanesulfonic acid (pH 5.7), 1 mM $MgCl_2$, 1 mM $CaCl_2$, 1 mM 2-mercaptoethanol and 0.1% (w/v) bovine serum albumin (Sigma-Aldrich). (Before the addition of $CaCl_2$, 2-mercaptoethanol and bovine serum albumin, the solution was heated to 55 °C for 10 min to inactivate proteases and facilitate enzyme solubility. Once the solution cooled to room temperature, $CaCl_2$, 2-mercaptoethanol and bovine serum albumin were added. Finally, sterile Milli-Q water was added to reach a final volume of 4 ml. The resulting enzyme solution was filtered through a 0.45 µm syringe filter and added to the 35 mm Petri dish.)

The tissues were kept under vacuum (30 kPa) for 30 min in the dark at room temperature. Tissue digestion was performed with gentle shaking (40 rpm on a platform shaker) in the dark at 28 °C for 2 hours. Following digestion, an equal volume of W5 solution (2 mM 2-(*N*-morpholino)ethanesulfonic acid adjusted to pH 5.7 with KOH, 154 mM NaCl, 125 mM $CaCl_2$ and 5 mM KCl) was added. The mixture was gently pipetted several times with a Pasteur pipette. Protoplasts that passed through a 40 µm cell strainer (Falcon) and a 30 µm cell strainer (pluriStrainer) were collected into a 14 ml round-bottom Falcon tube (Falcon) and pelleted by centrifugation at 100 *g* for 6 min at 4 °C with slow acceleration/braking. The supernatant was gently removed without disturbing the pellet, and the pellet was gently resuspended with 6 ml of cold W5 solution and washed twice using the same centrifugation conditions. The cells were resuspended in 3 ml of cold W5 solution. The tube was placed on ice for 30 min to facilitate the sedimentation of intact cells. The supernatant containing dead cells or debris was removed as much as possible using a Pasteur pipette. The pellet was resuspended in 500 µl of cold W5 solution and transferred to a 2 ml microcentrifuge tube. The protoplasts were stained with 10 µg ml^{-1} fluorescein diacetate to check cell concentration and viability with a haemocytometer under a fluorescent microscope. More than 20,000 high-quality protoplasts with viability ≥80% were immediately loaded onto the SCOPE-chip (Singleron) to collect single cells. Libraries were prepared according to the instructions of the GEXSCOPE single-cell RNA library kits (Singleron).

Single-cell RNA-seq analysis

The sequencing reads from two biological replicates of 6 mm B73 ears were aligned to the maize v.5 reference genome using the CeleScope bioinformatics analysis pipeline (v.1.6.1) available at https://github.com/singleron-RD/CeleScope. Probable doublets were removed using DoubletFinder[88]. After obtaining the single-cell raw expression matrix, we filtered out low-quality cells on the basis of the number of genes detected (<1,500 or >10,000) and excluded cells with a high percentage of mitochondrial genes (>5%) to avoid cytoplasmic RNA leakage. We also excluded the protoplasting-responsive genes identified in a previous study[16] to avoid potential confounding effects. Finally, we retained 19,584 single cells and 28,587 genes for downstream analysis.

Downstream analyses were mainly performed using the Seurat package (v.4.1.1)[50]. Normalized data were generated using the NormalizeData function (LogNormalize, scaling factor 10,000), and variable genes were detected using the FindVariableGenes function (vst method, 2,000 features). The scaled data were then subjected to PCA using the RunPCA function. To integrate multiple samples, we used the RunHarmony function to correct batch effects. Subsequently, an SNN graph was constructed, and cells were clustered with the Louvain method (using the FindNeighbors and FindClusters functions). Finally, the data were visualized using nonlinear dimensional reduction algorithms (using the RunUMAP function).

Integrating scRNA-seq and Stereo-seq data

The proportion of cells from different Sc-Clusters in the spots were estimated using the STRIDE deconvolve function[55]. The proportions of cells from different Sc-Clusters in the bin50s of sections 1 and 2 are listed in Supplementary Table 8, those from section 3 are listed in Supplementary Table 9 and those from section 4 are listed in Supplementary Table 10.

Co-expression network construction and GO and KEGG enrichment analysis

The gene co-expression network was constructed using the WGCNA package (v.1.71)[56]. We calculated the average expression level of genes

in each Sc-Cluster and used these as the input for WGCNA. After obtaining the gene modules and the weights of connection degrees between each gene on the basis of their expression patterns, we performed gene set enrichment analysis using the gProfiler web tool (https://biit.cs.ut.ee/gprofiler/gost). The network diagram was generated using Cytoscape (v.3.7.1)[60].

SNP heritability analysis

We used the LDAK software v.LD5.2 (ref. 89) to estimate narrow-sense heritability (h^2) from subsets of hub gene SNPs located 2 kb upstream and downstream. To test whether the heritability for a given trait was greater than expected by chance, we estimated the heritability for 1,000 permutations using a random subset of maize genes. Simultaneously, we computed the mean expression level of hub genes within each gene module (normalized expression level: module 3, 0.6051; module 5, 0.5120; module 7, 0.0929) to verify that the selected random genes exhibited expression levels surpassing the average expression level of these hub genes. For each permutation, genes with at least one SNP within the genic region were randomly selected to create a subset with a size within ±5 of the target set. A target set was considered significant for a given trait if its heritability exceeded the top 5% of permuted values.

Reporting summary

Further information on research design is available in the Nature Portfolio Reporting Summary linked to this article.

Data availability

The scRNA-seq and Stereo-seq data from this study can be found in CNGBdb (https://db.cngb.org/) and under project accession code CNP0004249 (https://db.cngb.org/search/project/CNP0004249/). Additional data, including the processed H5ad data, the original gene expression matrix and expression patterns of marker genes across all sections can be accessed at the STOmicsDB database[90], https://db.cngb.org/stomics/mdesta/. Source data are provided with this paper.

Code availability

The code for counting and annotating mapped reads is available via GitHub at https://github.com/BGIResearch/handleBam.

References

1. Tanaka, W., Pautler, M., Jackson, D. & Hirano, H. Y. Grass meristems II: inflorescence architecture, flower development and meristem fate. *Plant Cell Physiol.* **54**, 313–324 (2013).
2. Benlloch, R., Berbel, A., Serrano-Mislata, A. & Madueño, F. Floral initiation and inflorescence architecture: a comparative view. *Ann. Bot.* **100**, 659–676 (2007).
3. Irish, E. Class II tassel seed mutations provide evidence for multiple types of inflorescence meristems in maize (Poaceae). *Am. J. Bot.* **84**, 1502 (1997).
4. Jackson, D., Veit, B. & Hake, S. Expression of maize *KNOTTED1* related homeobox genes in the shoot apical meristem predicts patterns of morphogenesis in the vegetative shoot. *Development* **120**, 405–413 (1994).
5. Gallavotti, A. et al. The role of *barren stalk1* in the architecture of maize. *Nature* **432**, 630–635 (2004).
6. Vollbrecht, E., Springer, P. S., Goh, L., Buckler, E. S. T. & Martienssen, R. Architecture of floral branch systems in maize and related grasses. *Nature* **436**, 1119–1126 (2005).
7. Satoh-Nagasawa, N., Nagasawa, N., Malcomber, S., Sakai, H. & Jackson, D. A trehalose metabolic enzyme controls inflorescence architecture in maize. *Nature* **441**, 227–230 (2006).
8. Chuck, G., Muszynski, M., Kellogg, E., Hake, S. & Schmidt, R. J. The control of spikelet meristem identity by the *branched silkless1* gene in maize. *Science* **298**, 1238–1241 (2002).
9. Ning, Q. et al. An ethylene biosynthesis enzyme controls quantitative variation in maize ear length and kernel yield. *Nat. Commun.* **12**, 5832 (2021).
10. Luo, Y. et al. Genetic variation in *YIGE1* contributes to ear length and grain yield in maize. *N. Phytol.* **234**, 513–526 (2022).
11. Lloyd, J. & Meinke, D. A comprehensive dataset of genes with a loss-of-function mutant phenotype in *Arabidopsis*. *Plant Physiol.* **158**, 1115–1129 (2012).
12. Goldman, S. L. et al. The impact of heterogeneity on single-cell sequencing. *Front. Genet.* **10**, 8 (2019).
13. Zhang, T. Q., Chen, Y., Liu, Y., Lin, W. H. & Wang, J. W. Single-cell transcriptome atlas and chromatin accessibility landscape reveal differentiation trajectories in the rice root. *Nat. Commun.* **12**, 2053 (2021).
14. Zhang, T. Q., Chen, Y. & Wang, J. W. A single-cell analysis of the *Arabidopsis* vegetative shoot apex. *Dev. Cell* **56**, 1056–1074.e8 (2021).
15. Satterlee, J. W., Strable, J. & Scanlon, M. J. Plant stem-cell organization and differentiation at single-cell resolution. *Proc. Natl Acad. Sci. USA* **117**, 33689–33699 (2020).
16. Xu, X. et al. Single-cell RNA sequencing of developing maize ears facilitates functional analysis and trait candidate gene discovery. *Dev. Cell* **56**, 557–568.e6 (2021).
17. Ortiz-Ramírez, C. et al. Ground tissue circuitry regulates organ complexity in maize and *Setaria*. *Science* **374**, 1247–1252 (2021).
18. Chen, A. et al. Spatiotemporal transcriptomic atlas of mouse organogenesis using DNA nanoball-patterned arrays. *Cell* **185**, 1777–1792.e21 (2022).
19. Wei, X. et al. Single-cell Stereo-seq reveals induced progenitor cells involved in axolotl brain regeneration. *Science* **377**, eabp9444 (2022).
20. Liu, C. et al. Spatiotemporal mapping of gene expression landscapes and developmental trajectories during zebrafish embryogenesis. *Dev. Cell* **57**, 1284–1298.e5 (2022).
21. Xia, K. et al. The single-cell stereo-seq reveals region-specific cell subtypes and transcriptome profiling in *Arabidopsis* leaves. *Dev. Cell* **57**, 1299–1310.e4 (2022).
22. Liu, Y. et al. Spatial transcriptome analysis on peanut tissues shed light on cell heterogeneity of the peg. *Plant Biotechnol. J.* **20**, 1648–1650 (2022).
23. Song, X. et al. Spatial transcriptomics reveals light-induced chlorenchyma cells involved in promoting shoot regeneration in tomato callus. *Proc. Natl Acad. Sci. USA* **120**, e2310163120 (2023).
24. Liu, Z. et al. Integrated single-nucleus and spatial transcriptomics captures transitional states in soybean nodule maturation. *Nat. Plants* **9**, 515–524 (2023).
25. Vollbrecht, E. & Schmidt, R.J. in *Handbook of Maize: Its Biology* (eds Bennetzen, J. L. & Hake, S. C.) 13–40 (Springer New York, 2009).
26. Ambrose, B. A. et al. Molecular and genetic analyses of the *silky1* gene reveal conservation in floral organ specification between eudicots and monocots. *Mol. Cell* **5**, 569–579 (2000).
27. Bommert, P. et al. *thick tassel dwarf1* encodes a putative maize ortholog of the *Arabidopsis CLAVATA1* leucine-rich repeat receptor-like kinase. *Development* **132**, 1235–1245 (2005).
28. Bortiri, E. et al. *ramosa2* encodes a LATERAL ORGAN BOUNDARY domain protein that determines the fate of stem cells in branch meristems of maize. *Plant Cell* **18**, 574–585 (2006).
29. Chen, Z. et al. Structural variation at the maize *WUSCHEL1* locus alters stem cell organization in inflorescences. *Nat. Commun.* **12**, 2378 (2021).
30. Chuck, G., Meeley, R. & Hake, S. Floral meristem initiation and meristem cell fate are regulated by the maize *AP2* genes *ids1* and *sid1*. *Development* **135**, 3013–3019 (2008).

31. Chuck, G., Meeley, R. B. & Hake, S. The control of maize spikelet meristem fate by the *APETALA2*-like gene indeterminate *spikelet1*. *Genes Dev.* **12**, 1145–1154 (1998).
32. Chuck, G. S., Brown, P. J., Meeley, R. & Hake, S. Maize SBP-box transcription factors *unbranched2* and *unbranched3* affect yield traits by regulating the rate of lateral primordia initiation. *Proc. Natl Acad. Sci. USA* **111**, 18775–18780 (2014).
33. Gallavotti, A. et al. The control of axillary meristem fate in the maize *ramosa* pathway. *Development* **137**, 2849–2856 (2010).
34. Galli, M. et al. Auxin signaling modules regulate maize inflorescence architecture. *Proc. Natl Acad. Sci. USA* **112**, 13372–13377 (2015).
35. Kerstetter, R. A., Laudencia-Chingcuanco, D., Smith, L. G. & Hake, S. Loss-of-function mutations in the maize homeobox gene, *knotted1*, are defective in shoot meristem maintenance. *Development* **124**, 3045–3054 (1997).
36. Liu, R. et al. Fine mapping and candidate gene prediction of a pleiotropic quantitative trait locus for yield-related trait in *Zea mays*. *PLoS ONE* **7**, e49836 (2012).
37. Pautler, M. et al. *FASCIATED EAR4* encodes a bZIP transcription factor that regulates shoot meristem size in maize. *Plant Cell* **27**, 104–120 (2015).
38. Skirpan, A., Wu, X. & McSteen, P. Genetic and physical interaction suggest that BARREN STALK 1 is a target of BARREN INFLORESCENCE2 in maize inflorescence development. *Plant J.* **55**, 787–797 (2008).
39. Strable, J. & Vollbrecht, E. Maize *YABBY* genes *drooping leaf1* and *drooping leaf2* regulate floret development and floral meristem determinacy. *Development* **146**, dev171181 (2019).
40. Strable, J. et al. Maize *YABBY* genes *drooping leaf1* and *drooping leaf2* regulate plant architecture. *Plant Cell* **29**, 1622–1641 (2017).
41. Xu, G. et al. Complex genetic architecture underlies maize tassel domestication. *N. Phytol.* **214**, 852–864 (2017).
42. Zhang, D. et al. *GRF-interacting factor1* regulates shoot architecture and meristem determinacy in maize. *Plant Cell* **30**, 360–374 (2018).
43. Whipple, C. J. et al. A conserved mechanism of bract suppression in the grass family. *Plant Cell* **22**, 565–578 (2010).
44. Chuck, G., Whipple, C., Jackson, D. & Hake, S. The maize SBP-box transcription factor encoded by *tasselsheath4* regulates bract development and the establishment of meristem boundaries. *Development* **137**, 1243–1250 (2010).
45. Du, Y. et al. *UNBRANCHED3* expression and inflorescence development is mediated by *UNBRANCHED2* and the distal enhancer, *KRN4*, in maize. *PLoS Genet.* **16**, e1008764 (2020).
46. Jia, H. et al. A serine/threonine protein kinase encoding gene *KERNEL NUMBER PER ROW6* regulates maize grain yield. *Nat. Commun.* **11**, 988 (2020).
47. Xiao, Y. et al. Boundary domain genes were recruited to suppress bract growth and promote branching in maize. *Sci. Adv.* **8**, eabm6835 (2022).
48. Chuck, G. & Bortiri, E. The unique relationship between *tsh4* and *ra2* in patterning floral phytomers. *Plant Signal. Behav.* **5**, 979–981 (2010).
49. Bartlett, M. E. et al. The maize *PI/GLO* ortholog Zm*m16/sterile tassel silky ear1* interacts with the zygomorphy and sex determination pathways in flower development. *Plant Cell* **27**, 3081–3098 (2015).
50. Satija, R., Farrell, J. A., Gennert, D., Schier, A. F. & Regev, A. Spatial reconstruction of single-cell gene expression data. *Nat. Biotechnol.* **33**, 495–502 (2015).
51. Kim, D. E. et al. The impact of fasciation on maize inflorescence architecture. *J. Plant Biol.* **65**, 87–98 (2022).
52. Du, Y., Wu, B., Xing, Y. & Zhang, Z. Conservation and divergence: regulatory networks underlying reproductive branching in rice and maize. *J. Adv. Res.* **41**, 179–190 (2022).
53. Qiu, X. et al. Reversed graph embedding resolves complex single-cell trajectories. *Nat. Methods* **14**, 979–982 (2017).
54. Korsunsky, I. et al. Fast, sensitive and accurate integration of single-cell data with Harmony. *Nat. Methods* **16**, 1289–1296 (2019).
55. Sun, D., Liu, Z., Li, T., Wu, Q. & Wang, C. STRIDE: accurately decomposing and integrating spatial transcriptomics using single-cell RNA sequencing. *Nucleic Acids Res.* **50**, e42 (2022).
56. Langfelder, P. & Horvath, S. WGCNA: an R package for weighted correlation network analysis. *BMC Bioinform.* **9**, 559 (2008).
57. Douglas, C. J. Phenylpropanoid metabolism and lignin biosynthesis: from weeds to trees. *Trends Plant Sci.* **1**, 171–178 (1996).
58. Saha, P. et al. Phenylpropanoid biosynthesis gene expression precedes lignin accumulation during shoot development in lowland and upland switchgrass genotypes. *Front. Plant Sci.* **12**, 640930 (2021).
59. Suh, M. C. et al. Cuticular lipid composition, surface structure, and gene expression in *Arabidopsis* stem epidermis. *Plant Physiol.* **139**, 1649–1665 (2005).
60. Shannon, P. et al. Cytoscape: a software environment for integrated models of biomolecular interaction networks. *Genome Res.* **13**, 2498–2504 (2003).
61. Luo, B., Xue, X. Y., Hu, W. L., Wang, L. J. & Chen, X. Y. An ABC transporter gene of *Arabidopsis thaliana*, At*WBC11*, is involved in cuticle development and prevention of organ fusion. *Plant Cell Physiol.* **48**, 1790–1802 (2007).
62. Panikashvili, D. et al. The *Arabidopsis* DESPERADO/AtWBC11 transporter is required for cutin and wax secretion. *Plant Physiol.* **145**, 1345–1360 (2007).
63. Javelle, M. et al. Overexpression of the epidermis-specific homeodomain-leucine zipper IV transcription factor OUTER CELL LAYER1 in maize identifies target genes involved in lipid metabolism and cuticle biosynthesis. *Plant Physiol.* **154**, 273–286 (2010).
64. Todd, J., Post-Beittenmiller, D. & Jaworski, J. G. KCS1 encodes a fatty acid elongase 3-ketoacyl-CoA synthase affecting wax biosynthesis in *Arabidopsis thaliana*. *Plant J.* **17**, 119–130 (1999).
65. Sturaro, M. et al. Cloning and characterization of *GLOSSY1*, a maize gene involved in cuticle membrane and wax production. *Plant Physiol.* **138**, 478–489 (2005).
66. Wang, J. et al. Lignin engineering through laccase modification: a promising field for energy plant improvement. *Biotechnol. Biofuels* **8**, 145 (2015).
67. Zhao, Q. et al. Laccase is necessary and nonredundant with peroxidase for lignin polymerization during vascular development in *Arabidopsis*. *Plant Cell* **25**, 3976–3987 (2013).
68. Nuccio, M. L. et al. Expression of trehalose-6-phosphate phosphatase in maize ears improves yield in well-watered and drought conditions. *Nat. Biotechnol.* **33**, 862–869 (2015).
69. Kataya, A. R. A. et al. Multi-targeted trehalose-6-phosphate phosphatase I harbors a novel peroxisomal targeting signal 1 and is essential for flowering and development. *Planta* **251**, 98 (2020).
70. Li, Z. et al. The OsNAC23–Tre6P–SnRK1a feed-forward loop regulates sugar homeostasis and grain yield in rice. *Mol. Plant* **15**, 706–722 (2022).
71. Yang, X. et al. Characterization of a global germplasm collection and its potential utilization for analysis of complex quantitative traits in maize. *Mol. Breed.* **28**, 511–526 (2011).
72. Yang, N. et al. Genome wide association studies using a new nonparametric model reveal the genetic architecture of 17 agronomic traits in an enlarged maize association panel. *PLoS Genet.* **10**, e1004573 (2014).
73. Gui, S. et al. A pan-*Zea* genome map for enhancing maize improvement. *Genome Biol.* **23**, 178 (2022).
74. Li, M., Zhong, W., Yang, F. & Zhang, Z. Genetic and molecular mechanisms of quantitative trait loci controlling maize inflorescence architecture. *Plant Cell Physiol.* **59**, 448–457 (2018).

75. Liu, L. et al. Enhancing grain-yield-related traits by CRISPR–Cas9 promoter editing of maize *CLE* genes. *Nat. Plants* **7**, 287–294 (2021).
76. Wu, Q., Xu, F. & Jackson, D. All together now, a magical mystery tour of the maize shoot meristem. *Curr. Opin. Plant Biol.* **45**, 26–35 (2018).
77. Claeys, H. et al. Control of meristem determinacy by trehalose 6-phosphate phosphatases is uncoupled from enzymatic activity. *Nat. Plants* **5**, 352–357 (2019).
78. Hufford, M. B. et al. De novo assembly, annotation, and comparative analysis of 26 diverse maize genomes. *Science* **373**, 655–662 (2021).
79. Dobin, A. et al. STAR: ultrafast universal RNA-seq aligner. *Bioinformatics* **29**, 15–21 (2013).
80. Butler, A., Hoffman, P., Smibert, P., Papalexi, E. & Satija, R. Integrating single-cell transcriptomic data across different conditions, technologies, and species. *Nat. Biotechnol.* **36**, 411–420 (2018).
81. Stuart, T. et al. Comprehensive integration of single-cell data. *Cell* **177**, 1888–1902.e21 (2019).
82. Crow, M., Paul, A., Ballouz, S., Huang, Z. J. & Gillis, J. Characterizing the replicability of cell types defined by single cell RNA-sequencing data using MetaNeighbor. *Nat. Commun.* **9**, 884 (2018).
83. La Manno, G. et al. RNA velocity of single cells. *Nature* **560**, 494–498 (2018).
84. Wolf, F. A., Angerer, P. & Theis, F. J. SCANPY: large-scale single-cell gene expression data analysis. *Genome Biol.* **19**, 15 (2018).
85. Bergen, V., Lange, M., Peidli, S., Wolf, F. A. & Theis, F. J. Generalizing RNA velocity to transient cell states through dynamical modeling. *Nat. Biotechnol.* **38**, 1408–1414 (2020).
86. Tu, X. et al. Reconstructing the maize leaf regulatory network using ChIP-seq data of 104 transcription factors. *Nat. Commun.* **11**, 5089 (2020).
87. Yoo, S. D., Cho, Y. H. & Sheen, J. *Arabidopsis* mesophyll protoplasts: a versatile cell system for transient gene expression analysis. *Nat. Protoc.* **2**, 1565–1572 (2007).
88. McGinnis, C. S., Murrow, L. M. & Gartner, Z. J. DoubletFinder: doublet detection in single-cell RNA sequencing data using artificial nearest neighbors. *Cell Syst.* **8**, 329–337.e4 (2019).
89. Speed, D., Hemani, G., Johnson, M. R. & Balding, D. J. Improved heritability estimation from genome-wide SNPs. *Am. J. Hum. Genet.* **91**, 1011–1021 (2012).
90. Xu, Z. et al. STOmicsDB: a comprehensive database for spatial transcriptomics data sharing, analysis and visualization. *Nucleic Acids Res.* **5**, D1053–D1061 (2023).

Acknowledgements

This research was supported by funding from the National Key R&D Program of China (grant no. 2023ZD04073) to N.Y. and H.L., the National Natural Science Foundation of China (grant nos 32222062 and 32321005) and the National Key Laboratory of Crop Genetic Improvement Self-Research Program (grant no. ZW22B0102) to N.Y., the Outstanding Youth Team Cultivation Project of Center Universities (grant no. 2662023PY007) to L. Liu, the Shenzhen Science and Technology Program (grant no. KQTD20230301092839007) to H.L., the China Postdoctoral Science Foundation (grant no. 2023M731239) to Y. Luo, the National Key Research and Development Program of China (grant nos 2022YFD1201500 and 2020YFE0202300) to Jianbing Yan, and NSF-IOS grant no. 1934388 to D.J. Computation resources were provided by the high-throughput computing platform of the National Key Laboratory of Crop Genetic Improvement at Huazhong Agricultural University and supported by H.L. The construction of the spatial transcriptome visualization website is supported by the Guangdong Genomics Data Center (grant no. 2021B1212100001).

Author contributions

N.Y., L. Liu and H.L. conceived and supervised this study. Y.W., Y. Luo, X.G., Jiali Yan, W.S., L.C., Q.D., L. Li and L.Z. performed the library preparation and sequencing. Y.W., X.G., W.S., M.B. and W.W. performed the bioinformatics analysis. X.W., T.Y. and J.C. established the online database. Y. Li finished the transgenic and in situ experiments. Y.W., Y. Luo, X.G., Jiali Yan, Y. Li, D.J., Z.Z., X.X., Jianbing Yan, N.Y., L. Liu and H.L. discussed the data and prepared the manuscript. All authors read and approved the manuscript.

Competing interests

The authors declare no competing interests.

Additional information

Supplementary information The online version contains supplementary material available at https://doi.org/10.1038/s41477-024-01683-2.

Correspondence and requests for materials should be addressed to Huan Liu, Lei Liu or Ning Yang.

Peer review information *Nature Plants* thanks Clinton Whipple, Jixian Zhai and the other, anonymous, reviewer(s) for their contribution to the peer review of this work.

nature portfolio

Corresponding author(s): Ning Yang

Last updated by author(s): YYYY-MM-DD

Reporting Summary

Nature Portfolio wishes to improve the reproducibility of the work that we publish. This form provides structure for consistency and transparency in reporting. For further information on Nature Portfolio policies, see our Editorial Policies and the Editorial Policy Checklist.

Statistics

For all statistical analyses, confirm that the following items are present in the figure legend, table legend, main text, or Methods section.

n/a	Confirmed	
☐	☒	The exact sample size (*n*) for each experimental group/condition, given as a discrete number and unit of measurement
☐	☒	A statement on whether measurements were taken from distinct samples or whether the same sample was measured repeatedly
☐	☒	The statistical test(s) used AND whether they are one- or two-sided *Only common tests should be described solely by name; describe more complex techniques in the Methods section.*
☒	☐	A description of all covariates tested
☐	☒	A description of any assumptions or corrections, such as tests of normality and adjustment for multiple comparisons
☐	☒	A full description of the statistical parameters including central tendency (e.g. means) or other basic estimates (e.g. regression coefficient) AND variation (e.g. standard deviation) or associated estimates of uncertainty (e.g. confidence intervals)
☐	☒	For null hypothesis testing, the test statistic (e.g. *F*, *t*, *r*) with confidence intervals, effect sizes, degrees of freedom and *P* value noted *Give P values as exact values whenever suitable.*
☒	☐	For Bayesian analysis, information on the choice of priors and Markov chain Monte Carlo settings
☒	☐	For hierarchical and complex designs, identification of the appropriate level for tests and full reporting of outcomes
☒	☐	Estimates of effect sizes (e.g. Cohen's *d*, Pearson's *r*), indicating how they were calculated

Our web collection on statistics for biologists contains articles on many of the points above.

Software and code

Policy information about availability of computer code

Data collection	All sequencing library were prepared in house and raw reads were generated on illumina and DNBSEQ sequencing platform with manufacture's instruction. An expanded Stereo-seq and scRNA-seq data can be found in CNGBdb (https://db.cngb.org/), and under project accession code CNP0004249
Data analysis	Software used included: STAR (STAR/2.7.8a), DoubletFinder, R(4.1.3), Seurat package(4.1.1), Monocle2 (2.22.0), scanpy, scvelo, CeleScope (1.6.1), STRIDE, WGCNA(1.7.1), Cytoscape (3.7.1), LDAK(v5.2), MetaNeighbor(1.20.0)

For manuscripts utilizing custom algorithms or software that are central to the research but not yet described in published literature, software must be made available to editors and reviewers. We strongly encourage code deposition in a community repository (e.g. GitHub). See the Nature Portfolio guidelines for submitting code & software for further information.

Data

Policy information about availability of data

All manuscripts must include a data availability statement. This statement should provide the following information, where applicable:

- Accession codes, unique identifiers, or web links for publicly available datasets
- A description of any restrictions on data availability
- For clinical datasets or third party data, please ensure that the statement adheres to our policy

Stereo-seq and scRNA-seq data has been uploaded to CNGBdb (https://db.cngb.org/), and under project accession code CNP0004249

Research involving human participants, their data, or biological material

Policy information about studies with human participants or human data. See also policy information about sex, gender (identity/presentation), and sexual orientation and race, ethnicity and racism.

Reporting on sex and gender	No human participants or human data used in this study
Reporting on race, ethnicity, or other socially relevant groupings	No human participants or human data used in this study
Population characteristics	No human participants or human data used in this study
Recruitment	No human participants or human data used in this study
Ethics oversight	No human participants or human data used in this study

Note that full information on the approval of the study protocol must also be provided in the manuscript.

Field-specific reporting

Please select the one below that is the best fit for your research. If you are not sure, read the appropriate sections before making your selection.

☒ Life sciences ☐ Behavioural & social sciences ☐ Ecological, evolutionary & environmental sciences

For a reference copy of the document with all sections, see nature.com/documents/nr-reporting-summary-flat.pdf

Life sciences study design

All studies must disclose on these points even when the disclosure is negative.

Sample size	No sample size is calculated. The sample size is the number of individual.
Data exclusions	The threshold for filtering low-quality bins in Stereo-seq was set to no more than 150 or higher than 5000 gene counts. After filtering, the remaining bin50s were included in the downstream analysis. The threshold for filtering low-quality cells in scRNA-seq was set to no more than 1500 or higher than 10000 gene counts. After filtering, the remaining cells were included in the downstream analysis.
Replication	All experiment data was reliably reproduced in multiple independent experiments. There are three replications (three chips and four sections) in Stereo-seq and two replications in scRNA-seq.
Randomization	We used the LDAK software (v5.2) to estimate narrow-sense heritability from subsets of hub gene. To test if the heritability for a given trait was greater than expected by chance, we estimated the heritability for 1000 permutations using a random subset of maize genes. For each permutation, genes with at least one SNP within the genic region were randomly selected to create a subset with a size within ± 5 of the target set.
Blinding	No blinding was used.

Reporting for specific materials, systems and methods

We require information from authors about some types of materials, experimental systems and methods used in many studies. Here, indicate whether each material, system or method listed is relevant to your study. If you are not sure if a list item applies to your research, read the appropriate section before selecting a response.

Materials & experimental systems

n/a	Involved in the study
☒	☐ Antibodies
☒	☐ Eukaryotic cell lines
☒	☐ Palaeontology and archaeology
☒	☐ Animals and other organisms
☒	☐ Clinical data
☒	☐ Dual use research of concern
☐	☒ Plants

Methods

n/a	Involved in the study
☒	☐ ChIP-seq
☒	☐ Flow cytometry
☒	☐ MRI-based neuroimaging

Dual use research of concern

Policy information about dual use research of concern

Hazards

Could the accidental, deliberate or reckless misuse of agents or technologies generated in the work, or the application of information presented in the manuscript, pose a threat to:

No	Yes	
☒	☐	Public health
☒	☐	National security
☒	☐	Crops and/or livestock
☒	☐	Ecosystems
☒	☐	Any other significant area

Experiments of concern

Does the work involve any of these experiments of concern:

No	Yes	
☒	☐	Demonstrate how to render a vaccine ineffective
☒	☐	Confer resistance to therapeutically useful antibiotics or antiviral agents
☒	☐	Enhance the virulence of a pathogen or render a nonpathogen virulent
☒	☐	Increase transmissibility of a pathogen
☒	☐	Alter the host range of a pathogen
☒	☐	Enable evasion of diagnostic/detection modalities
☒	☐	Enable the weaponization of a biological agent or toxin
☒	☐	Any other potentially harmful combination of experiments and agents